INORGANIC CHEMISTRY FRONTIERS

RESEARCH ARTICLE

View Article Online
View Journal | View Issue

Cite this: *Inorg. Chem. Front.*, 2024, **11**, 4424

Chiral defect-induced blue photoluminescence and circularly polarized luminescence of zero-dimensional Cs_4PbBr_6 perovskite nanocrystals†

Jiaqi Zhao, Yuan Wang, Tinglei Wang and Yu Wang *

Received 23rd April 2024,
Accepted 8th June 2024

DOI: 10.1039/d4qi01006j

rsc.li/frontiers-inorganic

Chiral defect-induced strategy is employed to synthesize zero-dimensional (0D) chiral Cs_4PbBr_6 perovskite nanocrystals (NCs) with blue photoluminescence *via* a phase transition process. The chirality of the ground state of chiral Cs_4PbBr_6 perovskite NCs is confirmed by circular dichroism (CD) spectra, which shows the characteristic mirrored CD signals, behaving as a pair of enantiomers. Meanwhile, the obvious circularly polarized luminescence (CPL) response indicates that the chiral Cs_4PbBr_6 perovskite NCs are endowed with the chirality of the excited state. Furthermore, the UV–vis spectroscopy and electron paramagnetic resonance (EPR) data explicitly reveal that the CPL response originates from the chiral bromine vacancy (V_{Br}). This work not only provides guidance to realize the CPL of 0D chiral perovskites but also gives insights into the structure–property relationship.

1. Introduction

Chiral perovskites have attracted considerable attention due to their unique chiral and optoelectronic properties as well as their tremendous application in circularly polarized luminescence (CPL) photodetectors,[1,2] circularly polarized light-emitting diodes,[3,4] nonlinear optics,[5] chiral-induced spin selectivity (CISS),[4,6] and spintronics.[7,8] In general, there have been three strategies employed to obtain chiral perovskites: (1) chiral organic molecules are inserted into the crystal lattice to obtain one- or two-dimensional perovskites, which generally possess the chirality of the ground state with a large circular dichroism (CD) signal.[9,10] (2) Chiral distortion can be realized by modifying the surface of achiral perovskite nanocrystals (NCs) with chiral molecules.[11–14] (3) A high CPL response can be obtained by grafting achiral perovskites onto chiral templates, such as spiral silica,[15,16] chiral gels,[17] and polymers.[18] Although chiral perovskites show a strong CD signal, symmetry breaking generates an indirect-bandgap character, which generally leads to the fact that chiral perovskites cannot exhibit an obvious CPL response.[19,20]

Recently, some chiral perovskites with CPL properties have been synthesized. For example, Ye *et al.* synthesized core–shell structures by using a chiral perovskite ($(R$-/S-MBA$)_2PbBr_4$) as the shell and achiral $MAPbBr_3$ as the core, which exhibits obvious CPL activity and the dissymmetry factor of luminescence (g_{lum}) value is 4.0×10^{-3} at room temperature.[4] Because of the formation of heterojunctions, the chiral non-emission layer can transfer chirality to the emission center, which results in the chirality of the excited state.[4,6,21] Helically arranged $CsPbBr_3$ NCs on silica nanohelices can generate CD and CPL signals with a maximum g_{lum} dissymmetric factor up to 6×10^{-3}.[16] This indicates that the helical arrangement of achiral perovskite NCs can give rise to the chirality of the ground state and excited state due to a dipole interaction between these NCs.[16,17] Perovskite NCs can also exhibit CPL characteristics by attaching chiral ligands on their surface.[11–14,22] For example, Cao *et al.* attaches the chiral amino acid ligands onto the surface of $CsPbBr_3$ perovskite NCs. The chiral imprint on the surface of the perovskite NCs originates from the strong coordination.[11] In addition, our previous work found that defects in chiral perovskites can induce strong photoluminescence and exhibit a strong CPL response.[23] This result indicates that defects in chiral perovskites can give rise to strong photoluminescence and CPL because the chiral defects improve the recombination rate of the exciton. Thus, can CPL be realized by creating chiral defects in achiral perovskites?

In this work, zero-dimensional (0D) chiral Cs_4PbBr_6 NCs were successfully prepared by using a chiral amine as the inductive agent *via* a phase transition process. They show the same X-ray diffraction (XRD) pattern as achiral Cs_4PbBr_6 NCs, which indicates that they possess the same crystal structures. Chiral Cs_4PbBr_6 NCs not only exhibit a strong CD signal but also show an obvious CPL response. Therefore, chiral Cs_4PbBr_6 NCs are simultaneously endowed with the chirality of the ground and excited states. The UV–vis spectra show the exist-

State Key Laboratory of Inorganic Synthesis and Preparative Chemistry, College of Chemistry, Jilin University, 2699 Qianjin Street, Changchun 130012, China.
E-mail: wangyu@jlu.edu.cn

†Electronic supplementary information (ESI) available: NMR spectrum, FTIR Characterization, TRPL Data and other details. See DOI: https://doi.org/10.1039/d4qi01006j

ence of a chiral bromine vacancy (V_{Br}) in Cs_4PbBr_6, which is further confirmed by electron paramagnetic resonance (EPR) results. In addition, no chiral V_{Br} can be generated in the achiral Cs_4PbBr_6, indicating that the chiral amine resulted in the formation of chiral defects *via* phase transition. Chiral defects play an important role in the CPL response and strong PL. This work not only provides a new method for the synthesis of chiral perovskites with CPL response but also deepens our understanding of the structure–performance correlation.

2. Experimental section

2.1. Materials

All the chemicals were obtained from commercial suppliers and used without further purification. Lead bromide ($PbBr_2$, ≥99.0%), octadecene (ODE, 90%), cesium carbonate (Cs_2CO_3, 99%), oleic acid (OAc, 85%), oleylamine (OAm, ~80–90%), hydrobromic acid (HBr, ACS, 48%), (*S*)-(−)-α-methylbenzylamine (*S*-MBA, 99%, ee 98%), and (*R*)-(+)-α-methylbenzylamine (*R*-MBA, 99%, ee 98%) were purchased from Aladdin. Toluene (AR) was purchased from Tianjin Yuanli Chemical Co., Ltd.

2.2 Synthesis and purification $CsPbBr_3$ NCs[24]

Cs precursors were prepared by adding 0.32 g Cs_2CO_3, 2 mL OAc, and 32 mL ODE into a flask, drying for 30 min at 120 °C under vacuum conditions, and then heating to 150 °C until Cs_2CO_3 is completely dissolved. Then, 0.146 g $PbBr_2$, 20 mL ODE, 2 mL OAc, and 2 mL OAm were mixed into a flask and dried for 20 min at room temperature under vacuum conditions. The mixture was heated at 120 °C for 30 min, and then the temperature was raised to 150 °C and maintained for 10 min. Subsequently, 4 mL Cs precursor was rapidly injected. After injection for 15 s, the reaction was stopped by cooling in an ice-water bath. The crude solution was centrifuged at 11 000 rpm for 5 min and precipitated and dispersed in 20 mL toluene. The solution was centrifuged at 7500 rpm for 5 min to obtain the supernatant.

2.3. Synthesis and purification of chiral organic ammonium bromide *R*- and *S*-MBABr

R- and *S*-MBABr was prepared according to a previously reported approach.[25] Specifically, 10 mL *R*- and *S*-MBA and 12 mL HBr were added into anhydrous ethanol (15 mL) and stirred vigorously at 0 °C overnight. The *R*- and *S*-MBABr precipitate was obtained by evaporating the solution at 75 °C, washed thoroughly by ethanol, and recrystallized in ethyl acetate until colorless; then, it was dried under a vacuum at 40 °C for 24 h.

2.4. Synthesis of chiral precursor solution

The chiral precursor solution was prepared by ultrasonically mixing 0.020 g *R*- and *S*-MBABr, 0.017 g $PbBr_2$, 0.3 mL *R*- and *S*-MBA, 0.5 mL OAc, and 0.2 mL OAm in toluene.

2.5. Synthesis of chiral Cs_4PbBr_6 NCs

Here 600 μL of *R*-,*S* chiral precursor solution was mixed with 1 mL purified $CsPbBr_3$ NCs, and the mixture was sonicated for 45 min at 40 °C and then centrifuged at 11 000 rpm for 10 min. The precipitate was dispersed in 1.5 mL toluene for subsequent testing.

2.6. Synthesis and purification of achiral Cs_4PbBr_6 NCs[26]

Cs precursors were prepared by adding 0.4 g Cs_2CO_3, 1.5 mL OAc, and 15 mL ODE into a three-neck flask and drying for 60 min at 120 °C under vacuum conditions. Then, 0.056 g $PbBr_2$, 20 mL ODE, 2 mL OAc, and 2 mL OAm were added into a three-neck flask and dried for 10 min at room temperature under vacuum conditions. The mixture was heated at 120 °C for 60 min, and then the temperature was raised to 150 °C. Subsequently, 1.6 mL Cs precursor was rapidly injected. After injection, the reaction was stopped by cooling in an ice bath for 10 s. The crude solution was centrifuged at 12 000 rpm for 5 min and the precipitate was dispersed in 7.5 mL toluene. The solution was centrifuged at 12 000 rpm for 5 min to obtain the supernatant.

2.7. Characterization

The transmission electron microscopy (TEM) and high-resolution transmission electron microscopy (HRTEM) data were recorded on an FEI Tecnai G2 S-Twin F20 instrument with a field-emission gun operating at 200 kV. The crystal structures of the samples were measured by the X-ray diffraction (XRD) patterns, recorded on a Bruker D8 ADVANCE diffractometer (40 kV, 40 mA) equipped with Cu Kα radiation (λ = 1.5406 Å). The UV–vis absorption (UV) spectra were obtained from a Shimadzu UV-2450 spectrophotometer. The steady-state PL spectra were recorded on a HORIBA FLUOROMAX-4 spectrophotometer. The time-resolved PL decay and photoluminescence quantum yields (PLQYs) were obtained on an Edinburgh Instrument FLS920 spectrophotometer. The CD spectra and CPL spectra were measured by a Bio-Logic MOS-450 spectrometer and JASCO CPL-300 spectrometer, respectively. The Fourier-transform infrared (FTIR) spectra were recorded on an IFS-66V/S FT-IR spectrometer with KBr pellets. The X-ray photoelectron spectra (XPS) were obtained by an ESCALAB 250 Analytical XPS spectrometer with a monochromatic X-ray source (Al Kα, $h\nu$ = 1486.6 eV). The ^{1}H nuclear magnetic resonance (NMR) spectra were recorded on an NMR spectrometer (VNMRS 400 MHz, Agilent Technologies). The electron paramagnetic resonance (EPR) spectra were obtained using a Bruker 300 EPR spectrometer at room temperature.

3. Results and discussion

3.1. Morphology, structure, and optical and electronic properties

Pristine perovskite nanocrystals were synthesized *via* a traditional hot-injection approach in the presence of OAc and OAm ligands.[24] The TEM images reveal that a majority of them

have cubic morphology with an average size of 10 nm (Fig. S1 and 2†). The average d spacing of the lattice fringes measured from the HRTEM image is about 0.29 nm, agreeing with the (200) lattice plane of the cubic $CsPbBr_3$ phase (Fig. S2c†). The XRD pattern of the as-synthesized perovskite NCs is presented in Fig. S3.† The peaks at 15.1°, 21.6°, 26.5°, 30.6°, 37.8°, 43.9°, and 46.7° can be indexed to the (100), (110), (111), (200), (211), (220), and (300) reflections, respectively, of the cubic $CsPbBr_3$ structure (JCPDS no.54-0752).[27] Furthermore, the peaks at 12.69°, 22.4°, 25.4°and 30° for pristine perovskite NCs correspond to the (110), (300), (024), and (223) reflections, respectively, of the hexagonal Cs_4PbBr_6 phase (JCPDS no. 73-2478),[28] which implies the presence of Cs_4PbBr_6 NCs and the pristine perovskites are the mixture of $CsPbBr_3$ phase and Cs_4PbBr_6 phase with the $CsPbBr_3$ being in the majority. The UV–vis absorption and PL spectra show that the as-synthesized sample exhibits an absorption band at 485 nm and a strong green emission at 510 nm with an excitation wavelength at 365 nm (Fig. S4†).

The chiral Cs_4PbBr_6 NCs, labeled with *R*- and *S*-Cs_4PbBr_6, were synthesized by using *R*- and *S*-MBA as an inducer *via* the phase transition process. The synthesis diagram of chiral Cs_4PbBr_6 NCs is shown in Fig. 1a. Typically, the chirality can be transferred to the as-synthesized *R*- and *S*-Cs_4PbBr_6 NCs from the *R*- and *S*-MBA molecules in the phase transition process. The obtained *R*- and *S*-Cs_4PbBr_6 NCs have uniform rhombohedral morphology and high crystallinity with an average size of 20 nm (Fig. 2 and Fig. S5†). The HRTEM images show that the average d spacing of the lattice fringes is 0.32 nm, corresponding to the (131) plane of hexagonal Cs_4PbBr_6 (Fig. 2e and f), in agreement with the selected-area fast Fourier transformation (FFT) patterns (Fig. 2f inset and Fig. S6†). All of the XRD peaks correspond to the reflections of the hexagonal Cs_4PbBr_6 (JCPDS no. 73-2478), indicating that no impure phase was found (Fig. 2g).

The achiral Cs_4PbBr_6 perovskite NCs without PL were prepared by hot injection for comparison, named as N-Cs_4PbBr_6 (Fig. 1b and S7†). In contrast to N-Cs_4PbBr_6, *R*- and *S*-Cs_4PbBr_6 NCs exhibit strong blue luminescence (Fig. 2 h), which is

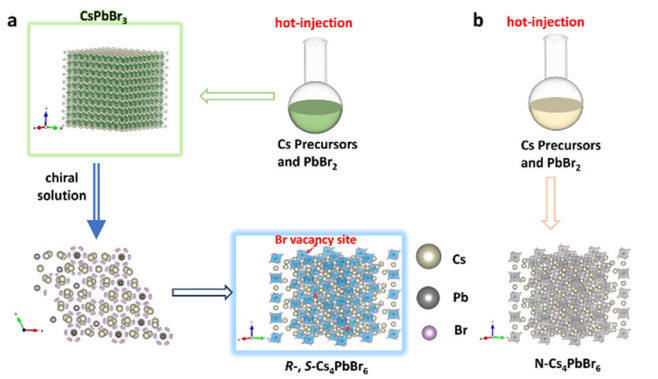

Fig. 1 (a) Schematic of the phase transformation from 3D cubic $CsPbBr_3$ to hexagonal 0D *R*- and *S*-Cs_4PbBr_6 NCs. (b) Schematic of the synthesis of N-Cs_4PbBr_6 NCs.

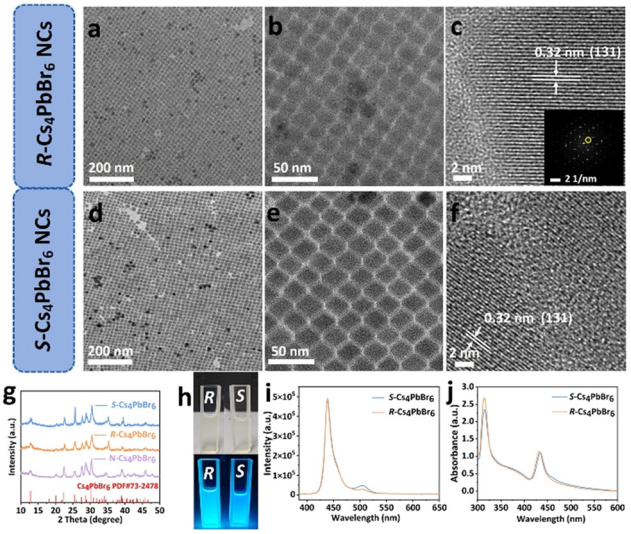

Fig. 2 TEM images of (a and b) *R*-Cs_4PbBr_6 NCs and (d and e) *S*-Cs_4PbBr_6 NCs with different magnifications. HRTEM images of (c) *R*-Cs_4PbBr_6 NCs and (f) *S*-Cs_4PbBr_6 NCs. The inset is the corresponding selected-area FFT patterns of *R*-Cs_4PbBr_6 NCs. (g) -XRD patterns of *R*- and *S*-Cs_4PbBr_6 NCs. (h) Photographs of *R*- and *S*-Cs_4PbBr_6 NCs under visible illumination (top) and UV illumination at 365 nm (bottom). (i) PL spectra of *R*- and *S*-Cs_4PbBr_6 NCs. (j) UV–vis spectra of *R*- and *S*-Cs_4PbBr_6 NCs.

obviously different from the as-synthesized $CsPbBr_3$ NCs with green luminescence (Fig. S8†). The *R*- and *S*-Cs_4PbBr_6 NCs display a strong PL emission peak at 438 nm and a very weak peak at 504 nm with an excitation wavelength at 365 nm (Fig. 2i). However, no emission can be detected for N-Cs_4PbBr_6NCs, in agreement with previous reports (Fig. S9a and S10†).[26,29] The decay curves of *R*- and *S*-Cs_4PbBr_6 NCs exhibit a triple-exponential decay and the average lifetimes are 42.10 and 50.36 ns, respectively (Fig. S11 and Table S1†). Furthermore, the PLQYs were determined to be 20% and 17% for *R*- and *S*-Cs_4PbBr_6 NCs, respectively. The PLQY and lifetime of N-Cs_4PbBr_6 NCs cannot be obtained because no PL signal could be detected. To investigate the unusual fluorescence emission phenomenon, the UV–vis absorption spectra of N-Cs_4PbBr_6 NCs and *R*- and *S*-Cs_4PbBr_6 NCs were measured (Fig. S9b† and Fig. 2j). N-Cs_4PbBr_6 NCs exhibit an exciton peak at around 313 nm, which originates from the intrinsic absorption of 0D Cs_4PbBr_6 NCs. The relative bandgap value is 3.81 eV, determined by Tauc fitting (Fig. S12†), consistent with the bandgap value of 0D Cs_4PbBr_6 NCs according to the previous reported value.[30] In contrast to N-Cs_4PbBr_6 NCs, the *R*- and *S*-Cs_4PbBr_6 NCs present a new exciton peak at 436 nm besides the peak at 313 nm. The relative bandgap value drops to 2.78 eV, which should be caused by the V_{Br} value in Cs_4PbBr_6 NCs in accordance with previous reports.[31–33]

3.2. Chiroptical property of *R*- and *S*-Cs_4PbBr_6 NCs

To evaluate the chiral optical properties of *R*- and *S*-Cs_4PbBr_6 NCs, the CD and CPL spectra were obtained, as shown in

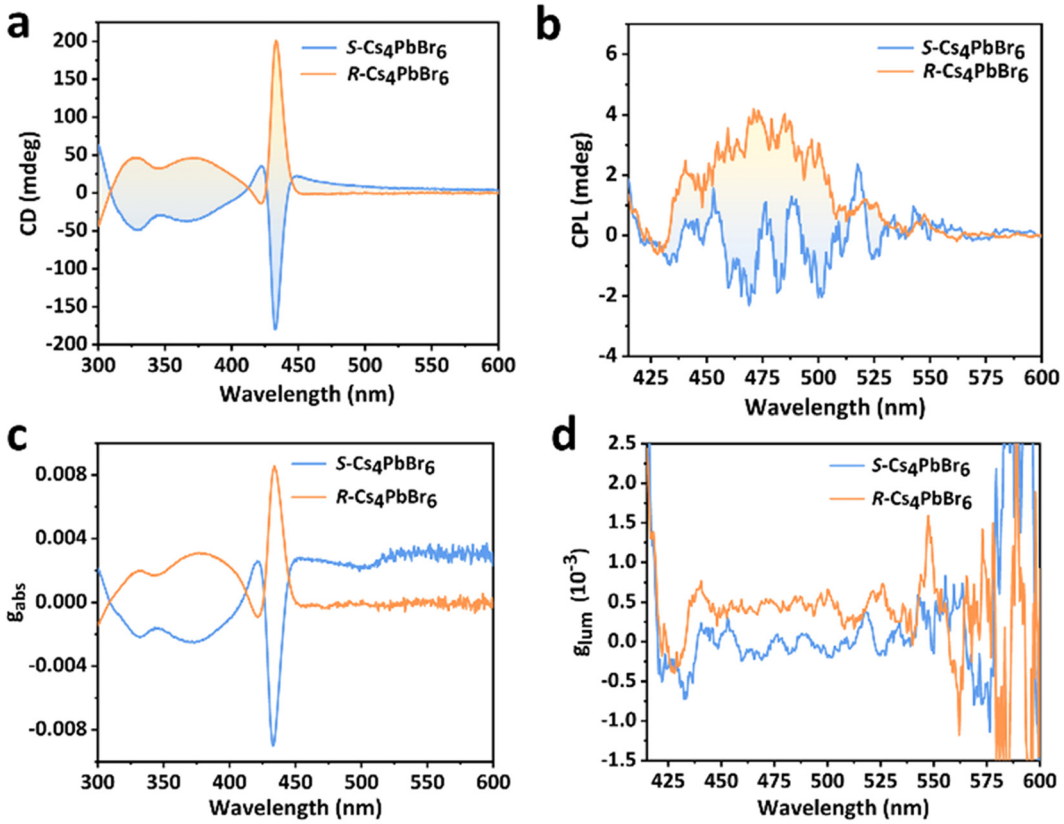

Fig. 3 Chiral characterization of *R*- and *S*-Cs_4PbBr_6 NCs. (a) CD spectra and (c) the corresponding dissymmetry factor g_{abs}. (b) CPL spectra and (d) g_{lum} of *R*- and *S*-Cs_4PbBr_6 NCs.

Fig. 3. The CD spectra evaluate the chirality of the ground states of *R*- and *S*-Cs_4PbBr_6 and N-Cs_4PbBr_6 NCs, and the intensity of CD can be quantified by the dissymmetry factor of absorption (g_{abs}).[34–36] The *R*- and *S*-Cs_4PbBr_6 NCs exhibit a characteristic mirror CD signal in the wavelength range of 300–450 nm, being different from that of *R*- and *S*-MBA (Fig. S13†). This result suggests that the relative absorption band should be attributed to the framework of chiral perovskites. This indicates that the chirality of *R*- and *S*-Cs_4PbBr_6 NCs originates from the relative chiral molecules, respectively, because no chirality can be obtained for the N-Cs_4PbBr_6 NCs and $CsPbBr_3$ (Fig. S14†). The g_{abs} values of the *R*- and *S*-Cs_4PbBr_6 NCs are similar to that of the CD spectra and the maximum values reach 8.5×10^{-3} and -8.8×10^{-3}, respectively, which agrees with the UV–vis absorption spectra. Furthermore, Fig. S15 and Table S2† present that the intensity of the CD signal and the g_{abs} spectra are closely related to the concentration of the chiral precursor solution. As the concentration of the chiral precursor increases, the intensity of CD and g_{abs} response first rises and then declines. The decrease in CD and g_{abs} at high concentration can be attributed to the replacement of long-chain alkyls by chiral ammonium and the stacking of high-concentration ligands.[24]

The CPL spectrum was used to evaluate the excited-state chirality of *R*- and *S*-Cs_4PbBr_6 and N-Cs_4PbBr_6 NCs. The N-Cs_4PbBr_6 NCs cannot exhibit a CPL response, confirming that they cannot be endowed with the chirality of the excited state. Compared with N-Cs_4PbBr_6 NCs, *R*- and *S*-Cs_4PbBr_6 NCs exhibit an obvious CPL response. Fig. 3b displays a mirror-like signal within the range from 425 to 525 nm, which can be observed for the *R*- and *S*-Cs_4PbBr_6 NCs. The asymmetry of CPL is quantified by the luminescence dissymmetry factor (g_{lum}),[29,34–36] being defined by $g_{lum} = (I_L - I_R)/(1/2(I_L + I_R))$, where I_L and I_R are the intensities of the left- and right-circularly polarized light components of the emission of chiral materials, respectively. The $|g_{lum}|$ value of the *R*- and *S*-Cs_4PbBr_6 NCs reach 6×10^{-4}, as shown in Fig. 3d. The corresponding DC (V) plots are shown in Fig. S16,† which match well with those of the CPL response. These results indicate that the *R*- and *S*-Cs_4PbBr_6 NCs possess the chirality of the excited state.

3.3. Structural transformation between $CsPbBr_3$ and Cs_4PbBr_6 NCs

To investigate the role of chiral amines, a series of experiments were performed. The content of the chiral amine was changed from 0 to 700 μL, where the content of perovskite NC precursors was maintained constant. The TEM images show that the cubic-phase $CsPbBr_3$ NCs gradually decreases with increasing content of chiral amine in the reaction medium, and all of the

$CsPbBr_3$ NCs were transformed into ordered rhombohedral Cs_4PbBr_6 NCs when the amount of chiral precursor was 600 μL (Fig. S17†). Consequently, the green emission gradually weakens and blue emission dominates the PL emission spectrum (Fig. S18a†). Meanwhile, the UV–vis spectrum exhibits an absorption band at around 490 nm, which gradually decreases and ultimately disappears, accompanied by a new sharp exciton absorption peak appearing at 435 nm (Fig. S18b†). This indicates that the NCs are changed from $CsPbBr_3$ to Cs_4PbBr_6. The corresponding XRD pattern shows that the diffraction peaks at 15° and 30.2° gradually disappear, confirming the presence of the phase transition from cubic $CsPbBr_3$ to rhombohedral chiral Cs_4PbBr_6 (Fig. S19†). The crystal structure of chiral Cs_4PbBr_6 NCs cannot be destroyed until the content of the chiral amine salts reaches 700 μL. These results unambiguously demonstrate that chiral amines play an important role in the phase transition process.

To better understand the growth of chiral Cs_4PbBr_6 NCs, the morphologies of NCs within different stages are tracked *via* TEM with the content of chiral amine salts being maintained constant in the reaction medium, as shown in Fig. 4. The cubic $CsPbBr_3$ NCs are gradually decomposed and they transform into the mixture of thin sheets and amorphous material. Subsequently, the homogenous chiral Cs_4PbBr_6 NCs are observed, which corresponds to a ligand-assisted dissolution–recrystallization mechanism and is consistent with the absorption spectra shown in Fig. 2j.[29,37,38] On the basis of the mechanism of dissolution–recrystallization, the $CsPbBr_3$ NCs decompose into the mixed solution including Pb^{2+}, Cs^+, and Br^- ions. Then, the Pb^{2+} cations can interact with Br^- anions to reform $[PbBr_6]^{4-}$ octahedrons. Finally, $[PbBr_6]^{4-}$ octahedrons interact with the Cs^+ and chiral amine cations to form the homogenously chiral Cs_4PbBr_6 NCs. The chiral amine can transfer its chirality into the chiral Cs_4PbBr_6 NCs in the recrystallization process.

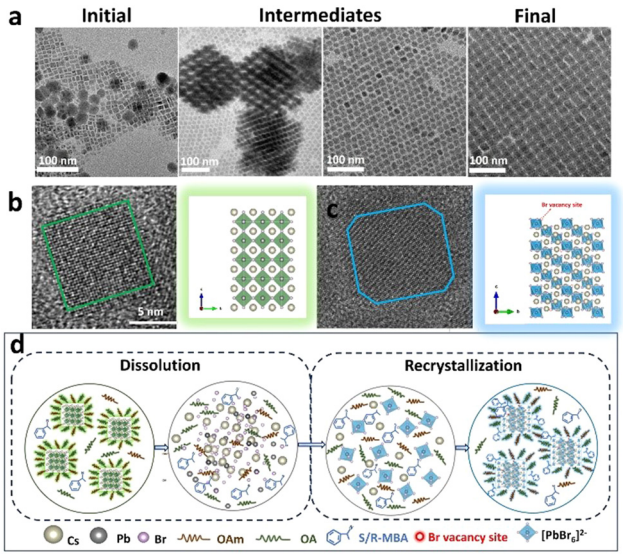

Fig. 4 Transient phases in the conversion of $CsPbBr_3$ to Cs_4PbBr_6: (a) TEM images of the initial Br perovskite NCs and of intermediates upon conversion to the final Cs_4PbBr_6 product. TEM images and atomic model (b) of cubic $CsPbBr_3$ (c) and of rhombohedral Cs_4PbBr_6NCs. (d) Schematic of the proposed dissolution–recrystallization transformation mechanism.

3.4. Surface bonding and microenvironment characteristics

In order to determine the origin of the PL and CPL signals of the *R*- and *S*-Cs_4PbBr_6 NCs, the surface-bonding characteristic of the chiral NCs was measured *via* FTIR and the microenvironment was investigated by XPS and NMR measurements. The FTIR spectra show that the adsorption peaks of the N-Cs_4PbBr_6 and *R*- and *S*-Cs_4PbBr_6 NCs are obviously different (Fig. S20†). The peaks at 1411 and 1714 cm^{-1} correspond to the symmetric stretching modes of COO^- and C═O of the OAc ligand for the N-Cs_4PbBr_6 and *R*- and *S*-Cs_4PbBr_6 NCs.[39,40] The absorption band at 2850–3000 cm^{-1} can be attributed to the vibration of C–Hx and the peaks centered at 3005, 1464, and 1379 cm^{-1} correspond to the C═C–H-stretching modes, C–H_2-bending mode, and C–H_3-bending mode, respectively, originating from the OAm and OAc ligands.[41,42] However, for the chiral Cs_4PbBr_6 NCs, the peaks at 724 and 764 cm^{-1} can be attributed to the C–H-rocking mode and the stretching of the primary amine group as well as out-of-plane C–H-bending vibrations of monosubstituted benzene. This result confirms the presence of chiral MBA ligands.[13,43]

The XPS data have been used to study the surface chemistry and elemental distribution. The XPS spectra of C, N, and Br of the N-Cs_4PbBr_6 and *R*- and *S*-Cs_4PbBr_6 NCs are shown in Fig. S21.† The C 1s peaks of N-Cs_4PbBr_6 are a doublet with binding energies of 286.2 and 284.8 eV, corresponding to the C–N/C–O and C–C of OAm/OAc, respectively. In contrast to N-Cs4$PbBr_6$, the C 1s spectrum of *R*- and *S*-Cs_4PbBr_6 is a triplet with binding energies of 288.3, 286.2, and 284.8 eV, being attributed to the π–π satellite, C–N/C–O, and C–C, respectively, confirming the existence of chiral amine on the surface of *R*- and *S*-Cs_4PbBr_6.[24,44] All the N 1s peaks of the N-Cs_4PbBr_6 and *R*- and *S*-Cs_4PbBr_6 NCs are doublets with binding energies of 399.6 and 401.4 eV and 399.8 and 401.7 eV, respectively, which correspond to C–NH_2 and C–NH_3^+, respectively. The ratios of C–NH_3^+ to C–NH_2 of *R*- and *S*-Cs_4PbBr_6 are higher than that of N-Cs_4PbBr_6, indicating that the protonated chiral amine exhibits stronger interaction with the surface of Cs_4PbBr_6 than that of OAm.[24,44] The Br 3d peaks of N-Cs_4PbBr_6 is a doublet with binding energies of 67.9 and 69 eV, which can be attributed to the inner Br^- and surface Br^-, respectively. Compared with N-Cs_4PbBr_6, although the Br 3d peaks of the *R*- and *S*-Cs_4PbBr_6 is also a doublet, the peaks show a shift of 0.35 and 0.2 eV towards a higher binding energy, respectively. In addition, the ratio of surface Br^- to inner Br^- of N-Cs_4PbBr_6, *S*-Cs_4PbBr_6 and *R*-Cs_4PbBr_6 are 0.95, 0.78, and 0.69, respectively, indicating the existence of chiral V_{Br} in *R*- and *S*-Cs_4PbBr_6 NCs, according to previous reports.[45]

The NMR measurement was performed to further confirm the action of chiral amine. To eliminate the interference of toluene in the reaction system, the products of N-Cs_4PbBr_6 and

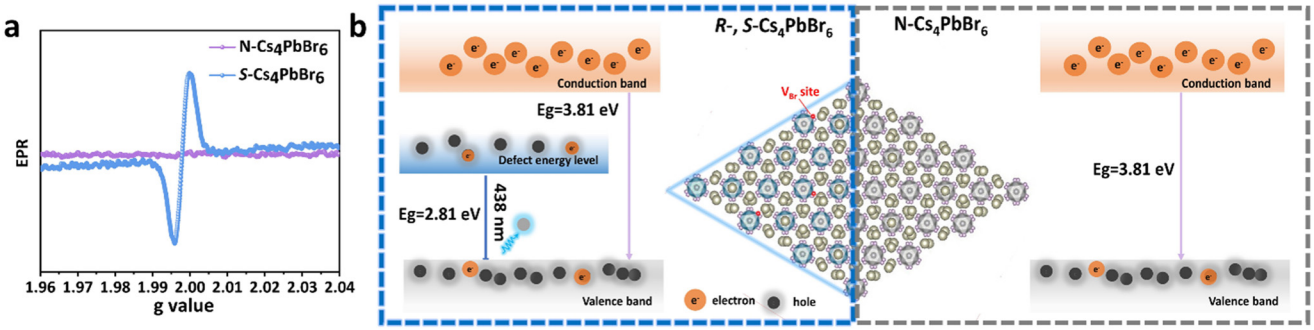

Fig. 5 (a) EPR spectra of *S*-Cs_4PbBr_6 NCs and N-Cs_4PbBr_6 NCs. (b) Schematic of the comparison of electronic band structure and luminescence mechanism for chiral Cs_4PbBr_6 NCs (left) and N-Cs_4PbBr_6 NCs (right).

S-Cs_4PbBr_6 NCs were rinsed by chloroform. The ^{1}H NMR spectra of chiral ligand *S*-MBA, N-Cs_4PbBr_6, and *S*-Cs_4PbBr_6 NCs are shown in Fig. S22.† The N-Cs_4PbBr_6 and *S*-Cs_4PbBr_6 NCs show the chemical-shift (δ) peaks at 0.86, 1.22–1.48, 1.62, 2.0, 2.3, and 5.3 ppm, confirming the presence of OAm/OAc, according to previous literature.[46] However, *S*-Cs_4PbBr_6 NCs exhibit some distinct peaks at $\delta \approx$ ~7.0–7.3 ppm and a faint peak at 4.49 ppm and 1.7 ppm, which is similar to that of *S*-MBA. This further indicates that a chiral amine can interact with the surface of chiral Cs_4PbBr_6 NCs and induce the formation of chiral V_{Br}. According to the abovementioned results, a possible mechanism for the formation of a chiral defect *via* the phase transition from cubic $CsPbBr_3$ to rhombohedral Cs_4PbBr_6 NCs is illustrated in Fig. 4d.

3.5. EPR measurement and CPL mechanism

The N-Cs_4PbBr_6 is a wide-bandgap direct semiconductor with a high bandgap of 3.81 eV and cannot show the exciton transition to the band in the visible region, as shown in Fig. S12.† However, chiral Cs_4PbBr_6 shows a new bandgap peak at around 2.78 eV, indicating that the blue emission comes from an intermediate state generated by chiral V_{Br}, rather than an intrinsic transition. To further prove that the emission originates from the chiral V_{Br}, the EPR spectrum was obtained for *S*-Cs_4PbBr_6 and N-Cs_4PbBr_6.

Fig. 5a exhibits that the single Lorentzian line centered at g = 1.998 can be observed for chiral Cs_4PbBr_6 NCs, and no EPR signal can be observed for N-Cs_4PbBr_6 NCs. This suggests that chiral bromine defects can be generated in the phase transition process for chiral Cs_4PbBr_6 NCs, which serves as a trap state to trap electrons to recombine with holes to form exciton centers.[32,33,47] Furthermore, the chirality of defects originates from the chiral amine, which not only generates a strong blue emission but also gives rise to a CPL response. The relative mechanism is illustrated in Fig. 5b.

4. Conclusions

In summary, the 0D *R*- and *S*-Cs_4PbBr_6 perovskite NCs have been successfully designed and synthesized *via* a phase transition process. These chiral Cs_4PbBr_6 NCs not only exhibit a significant PL but also show characteristic CD signals and obvious CPL response. The UV–vis, XPS, and EPR spectra further verify that the strong blue emission and CPL response originates from the chiral bromine defects. This work not only provides a new direction for the research of CPL functional materials but also gives insights into the structure–property relationship.

Author contributions

Jiaqi Zhao: investigation, conceptualization, data curation, methodology, formal analysis, writing – original draft. Yuan Wang: investigation, methodology, validation. Tinglei Wang: investigation, methodology, validation. Yu Wang: supervision, writing – review & editing. All authors have given approval to the final version of the manuscript.

Conflicts of interest

There are no conflicts to declare.

Acknowledgements

This work was financially supported by the National Natural Science Foundation of China Natural (no. 21771083).

References

1 T. Liu, W. Shi, W. Tang, Z. Liu, B. C. Schroeder, O. Fenwick and M. J. Fuchter, High responsivity circular polarized light detectors based on quasi two-dimensional chiral perovskite films, *ACS Nano*, 2022, **16**(2), 2682–2689.
2 C. Chen, L. Gao, W. Gao, C. Ge, X. Du, Z. Li, Y. Yang, G. Niu and J. Tang, Circularly polarized light detection using chiral hybrid perovskite, *Nat. Commun.*, 2019, **10**(1), 1927.

3 C.-H. Yang, S.-B. Xiao, H. Xiao, L.-J. Xu and Z.-N. Chen, Efficient Red-Emissive Circularly Polarized Electroluminescence Enabled by Quasi-2D Perovskite with Chiral Spacer Cation, *ACS Nano*, 2023, **17**(8), 7830–7836.
4 C. Ye, J. Jiang, S. Zou, W. Mi and Y. Xiao, Core-Shell Three-Dimensional Perovskite Nanocrystals with Chiral-Induced Spin Selectivity for Room-Temperature Spin Light-Emitting Diodes, *J. Am. Chem. Soc.*, 2022, **144**(22), 9707–9714.
5 C. Yuan, X. Li, S. Semin, Y. Feng, T. Rasing and J. Xu, Chiral lead halide perovskite nanowires for second-order nonlinear optics, *Nano Lett.*, 2018, **18**(9), 5411–5417.
6 Y.-H. Kim, Y. Zhai, H. Lu, X. Pan, C. Xiao, E. A. Gaulding, S. P. Harvey, J. J. Berry, Z. V. Vardeny, J. M. Luther and M. C. Beard, Chiral-induced spin selectivity enables a room-temperature spin light-emitting diode, *Science*, 2021, **371**, 1129–1133.
7 Q. Wei and Z. Ning, Chiral perovskite spin-optoelectronics and spintronics: toward judicious design and application, *ACS Mater. Lett.*, 2021, **3**(9), 1266–1275.
8 J. Wang, B. Mao and Z. V. Vardeny, Chirality induced spin selectivity in chiral hybrid organic–inorganic perovskites, *J. Chem. Phys.*, 2023, **159**(9), 091002.
9 J. Ma, C. Fang, C. Chen, L. Jin, J. Wang, S. Wang, J. Tang and D. Li, Chiral 2D perovskites with a high degree of circularly polarized photoluminescence, *ACS Nano*, 2019, **13**(3), 3659–3665.
10 Z. Li, Y. Yan, M. S. Song, J. Y. Xin, H.-Y. Wang, H. Wang and Y. Wang, Exciton–Phonon Coupling of Chiral One-Dimensional Lead-Free Hybrid Metal Halides at Room Temperature, *J. Phys. Chem. Lett.*, 2022, **13**, 4073–4081.
11 S. Chen, J. Fu, C. Zhang, Y. Hu, Y. Qiu, J. Chen, Q. Zhang and M. Cao, Chiral Multidentate Ligand Facilitating Perovskite Nanocrystals with Circularly Polarized Luminescence and Chiral Assembly, *Adv. Opt. Mater.*, 2024, 2302883.
12 Y. Wu, T. Zhao, X. Shao, J. Chen, T. Zhang, B. Li and S. Jiang, Ligand-assisted self-assembly of 3D perovskite nanocrystals into chiral inorganic quasi-2D perovskites (n= 3) with ligand-ratio-dependent chirality inversion, *Small*, 2023, **19**(36), 2301034.
13 B. Tang, S. Wang, H. Liu, N. Mou, A. S. Portniagin, P. Chen, Y. Wu, X. Gao, D. Lei and A. L. Rogach, Chiral Ligand-Induced Inversion and Tuning of Excitonic Optical Activity in Intrinsically Chiral $CsPbBr_3$ Perovskite Nanoplatelets, *Adv. Opt. Mater.*, 2024, **12**(4), 2301524.
14 C. Yang, S. Xiao, H. Xiao, L. Xu and Z. Chen, Efficient Red-Emissive Circularly Polarized Electroluminescence Enabled by Quasi-2D Perovskite with Chiral Spacer Cation, *ACS Nano*, 2023, **17**(8), 7830–7836.
15 Z. Li, Y. Yan, W. Y. Ma, J. Q. Zhao, Y. Fan and Y. Wang, Chirality Transfer from Chiral Mesoporous Silica to Perovskite $CsPbBr_3$ Nanocrystals: The Role of Chiral Confinement, *CCS Chem.*, 2022, **4**, 3447–3454.
16 P. Liu, W. Chen, Y. Okazaki, Y. Battie, L. Brocard, M. Decossas, E. Pouget, P. Müller-Buschbaum, B. Kauffmann, S. Pathan, T. Sagawa and R. Oda, Optically active perovskite $CsPbBr_3$ nanocrystals helically arranged on inorganic silica nanohelices, *Nano Lett.*, 2020, **20**(12), 8453–8460.
17 Y. Shi, P. Duan, S. Huo, Y. Li and M. Liu, Endowing perovskite nanocrystals with circularly polarized luminescence, *Adv. Mater.*, 2018, **30**(12), 1705011.
18 Z. Wen, R. Lu, F. Gu, K. Zheng, L. Zhang, H. Jin, Y. Chen, S. Wang and S. Pan, Enabling Efficient Blue-Emissive Circularly Polarized Luminescence by In Situ Crafting of Chiral Quasi-2D Perovskite Nanosheets within Polymer Nanofibers, *Adv. Funct. Mater.*, 2023, **33**(7), 2212095.
19 W. Tao, Q. Zhou and H. Zhu, Dynamic polaronic screening for anomalous exciton spin relaxation in two-dimensional lead halide perovskites, *Sci. Adv.*, 2020, **6**(47), eabb7132.
20 G. Xing, B. Wu, X. Wu, M. Li, B. Du, Q. Wei, J. Guo, E. K. Yeow, T. C. Sum and W. Huang, Transcending the slow bimolecular recombination in lead-halide perovskites for electroluminescence, *Nat. Commun.*, 2017, **8**(1), 14558.
21 G. Jang, D. Y. Jo, S. Ma, J. Lee, J. Son, C. U. Lee, W. Jeong, S. Yang, J. H. Park, H. Yang and J. Moon, Core-Shell Perovskite Quantum Dots for Highly Selective Room-Temperature Spin Light–Emitting Diodes, *Adv. Mater.*, 2024, 2309335.
22 Y. H. Kim, Y. Zhai, E. A. Gaulding, S. N. Habisreutinger, T. Moot, B. A. Rosales and J. M. Luther, Strategies to achieve high circularly polarized luminescence from colloidal organic-inorganic hybrid perovskite nanocrystals, *ACS Nano*, 2020, **14**(7), 8816–8825.
23 J. Zhao, Y. Yan, Z. Li, Y. Wang, T. Wang and Y. Wang, Defect-Induced Circularly Polarized Luminescence of Chiral Perovskite Films, *J. Phys. Chem. C*, 2023, **127**(51), 24706–24712.
24 S. Jiang, Y. Song, H. Kang, B. Li, K. Yang, G. Xing, Y. Yu, S. Li, P. Zhao and T. Zhang, Ligand exchange strategy to achieve chiral perovskite nanocrystals with a high photoluminescence quantum yield and regulation of the chiroptical property, *ACS Appl. Mater. Interfaces*, 2021, **14**(2), 3385–3394.
25 Z. N. Georgieva, B. P. Bloom, S. Ghosh and D. H. Waldeck, Imprinting chirality onto the electronic states of colloidal perovskite nanoplatelets, *Adv. Mater.*, 2018, **30**(23), 1800097.
26 S. Zou, C. Liu, R. Li, F. Jiang, X. Chen, Y. Liu and M. Hong, From Nonluminescent to Blue-Emitting Cs_4PbBr_6 Nanocrystals: Tailoring the Insulator Bandgap of 0D Perovskite through Sn Cation Doping, *Adv. Mater.*, 2019, **31**(24), 1900606.
27 R. Yuan, L. Shen, C. Shen, J. Liu, L. Zhou, W. Xiang and X. Liang, $CsPbBr_3$: xEu^{3+} perovskite QD borosilicate glass: a new member of the luminescent material family, *Chem. Commun.*, 2018, **54**(27), 3395–3398.
28 X. Peng, J. Chen, F. Wang, C. Zhang and B. Yang, One-pot synthesis of $CsPbBr_3/Cs_4PbBr_6$ perovskite composite, *Optik*, 2020, **208**, 164579.
29 Z. Liu, Y. Bekenstein, X. Ye, S. C. Nguyen, J. Swabeck, D. Zhang, S.T Lee, P. Yang, W. Ma and A. P. Alivisatos,

Ligand mediated transformation of cesium lead bromide perovskite nanocrystals to lead depleted Cs_4PbBr_6 nanocrystals, *J. Am. Chem. Soc.*, 2017, **139**(15), 5309–5312.

30 Q. A. Akkerman, S. Park, E. Radicchi, F. Nunzi, E. Mosconi, F. De Angelis, R. Brescia, P. Rastogi, M. Prato and L. Manna, Nearly monodisperse insulator Cs_4PbX_6 (X= Cl, Br, I) nanocrystals, their mixed halide compositions, and their transformation into CsPbX3 nanocrystals, *Nano Lett.*, 2017, **17**(3), 1924–1930.

31 Y. Yuan, Q. Yao, J. Zhang, K. Wang, W. Zhang, T. Zhou, H. Sun and J. Ding, Negative photoconductivity in Cs_4PbBr_6 single crystal, *Phys. Chem. Chem. Phys.*, 2020, **22**(25), 14276–14283.

32 X. Liu, W. Xie, Y. Lu, X. Wang, S. Xu and J. Zhang, Water-induced ultrastrong green emission in Cs_4PbBr_6 quantum dot glass, *J. Mater. Chem. C*, 2022, **10**(2), 762–767.

33 J. H. Cha, H. J. Lee, S. H. Kim, K. C. Ko, B. J. Suh, O. H. Han and D. Y. Jung, Superparamagnetism of green emissive Cs_4PbBr_6 zero-dimensional perovskite crystals, *ACS Energy Lett.*, 2020, **5**(7), 2208–2216.

34 L. S. Yang, E. C. Lin, Y.-H. Hua, C. A. Hsu, H. Z. Chiu, P. H. Lo and Y. C. Chao, Circularly Polarized Photoluminescence of Chiral 2D Halide Perovskites at Room Temperature, *ACS Appl. Mater. Interfaces*, 2022, **14**, 54090–54100.

35 L. T. Tao, H. M. Zhan, Y. X. Cheng, C. J. Qin and L. X. Wang, Enhanced Circularly Polarized Photoluminescence of Chiral Perovskite Films by Surface Passivation with Chiral Amines, *J. Phys. Chem. Lett.*, 2023, **14**, 2317–2322.

36 D. D. Nuzzo, L. S. Cui, J. L. Greenfield, B. D. Zhao, R. H. Friend, S. C. Meskers and J. Circularly, Polarized Photoluminescence from Chiral Perovskite Thin Films at Room Temperature, *ACS Nano*, 2020, **14**, 7610–7616.

37 T. Udayabhaskararao, L. Houben, H. Cohen, M. Menahem, I. Pinkas, L. Avram, T. Wolf, A. Teitelboim, M. Leskes, O. Yaffe, M. Kazes, *et al.* A mechanistic study of phase transformation in perovskite nanocrystals driven by ligand passivation, *Chem. Mater.*, 2018, **30**(1), 84–93.

38 R. Yun, H. Yang, Y. Li, Y. Liu, Y. Chu, S. Wu, X. Liu, X. Zhang and X. Li, Inorganic Ligand Triggered Transformation from Cs_4PbBr_6 Nanocrystals to Blue-Emitting $CsPbBr_3$ Nanoplatelets, *Chem. Mater.*, 2022, **35**(2), 424–431.

39 I. Liascukiene, N. Aissaoui, S. J. Asadauskas, J. Landoulsi and J. F. Lambert, Ordered nanostructures on a hydroxylated aluminum surface through the self-assembly of fatty acids, *Langmuir*, 2012, **28**(11), 5116–5124.

40 S. Peng, Z. Wen, T. Ye, X. Xiao, K. Wang, J. Xia, J. Sun, T. Zhang, G. Mei, H. Liu, B. Xu, X. Li, R. Chen, G. Xing, K. Wang and Z. Tang, Effective surface ligand-concentration tuning of deep-blue luminescent $FAPbBr_3$ nanoplatelets with enhanced stability and charge transport, *ACS Appl. Mater. Interfaces*, 2020, **12**(28), 31863–31874.

41 S. Ding, M. Hao, C. Fu, T. Lin, A. Baktash, P. Chen, D. C. He, C. X. Zhang, W. J. Chen, A. K. Whittaker and Y. Bai, In situ bonding regulation of surface ligands for efficient and stable $FAPbI_3$ quantum dot solar cells, *Adv. Sci.*, 2022, **9**(35), 2204476.

42 B. Hou, D. Benito-Alifonso, R. Webster, D. Cherns, M. C. Galan and D. J. Fermín, Rapid phosphine-free synthesis of CdSe quantum dots: promoting the generation of Se precursors using a radical initiator, *J. Mater. Chem. A*, 2014, **2**(19), 6879–6886.

43 C. O. Sánchez, P. Sobarzo and N. Gatica, Electronic and structural properties of polymers based on phenylene vinylene and thiophene units. Control of the gap by gradual increases of thiophene moieties, *New J. Chem.*, 2015, **39**(10), 7979–7987.

44 G. H. Debnath, Z. N. Georgieva, B. P. Bloom, S. D. Tan and H. Waldeck, Using post-synthetic ligand modification to imprint chirality onto the electronic states of cesium lead bromide ($CsPbBr_3$) perovskite nanoparticles, *Nanoscale*, 2021, **13**(36), 15248–15256.

45 K. Dave, Z. Bao, S. Nakahara, K. Ohara, S. Masada, H. Tahara, Y. Kanemitsu and R. S. Liu, Improvement in quantum yield by suppression of trions in room temperature synthesized $CsPbBr_3$ perovskite quantum dots for backlight displays, *Nanoscale*, 2020, **12**(6), 3820–3826.

46 Y. H. Kim, R. Song, J. Hao, Y. Zhai, L. Yan, T. Moot, A. F. Palmstrom, R. Brunecky, W. You, J. M. Luther, *et al.* The structural origin of chiroptical properties in perovskite nanocrystals with chiral organic ligands, *Adv. Funct. Mater.*, 2022, **32**(25), 2200454.

47 Y. Lu, X. Liu, P. Li, Y. Duan, S. Xu and J. Zhang, Origin of Radioluminescence in Low-Dimensional Halide Perovskite Glass Ceramics under X-ray Excitation, *J. Phys. Chem. C*, 2021, **125**(49), 27497–27503.